Particle-Hole Asymmetry and Pinball Liquid in a Triangular-Lattice Extended Hubbard Model within Mean-Field Approximation

Aleksey Alekseev,[1, *] Agnieszka Cichy,[1, 2, †] and Konrad Jerzy Kapcia[1, ‡]

[1]*Institute of Spintronics and Quantum Information, Faculty of Physics and Astronomy,*
Adam Mickiewicz University in Poznań, Uniwersytetu Poznańskiego 2, PL-61614 Poznań, Poland
[2]*Institut für Physik, Johannes Gutenberg-Universität Mainz, Staudingerweg 9, D-55099 Mainz, Germany*

(Dated: April 30, 2025)

Recently, triangular lattice models have received a lot of attention since they can describe a number of strongly-correlated materials that exhibit superconductivity and various magnetic and charge orders. In this research we present an extensive analysis of the charge-ordering phenomenon of the triangular-lattice extended Hubbard model with repulsive onsite and nearest-neighbor interaction, arbitrary charge concentration, and $\sqrt{3} \times \sqrt{3}$ supercell (3-sublattice assumption). The model is solved in the ground state with the mean-field approximation which allowed to identify 8 charge-ordered phases and a large variety of phase transitions. An exotic pinball-liquid phase was found and described. Moreover, strong particle-hole asymmetry of the phase diagram is found to play an important role for triangular lattices. The analysis of band structures, unavailable for more advanced methods that take into account correlation effects, provided a great insight in the nature of triangular-lattice phases and phase transitions. The complexity of the mean-field phase diagram showed the importance and usefulness of the results for the further research with correlation effects included. Together with atomic-limit approximation it can serve them as both a starting point, and a tool to interpret results.

I. INTRODUCTION

2D triangular lattice is typical for a number of organic conductors, transition-metal oxides and dichalcogenides, can be formed by adsorbed helium atoms on a surface, and can describe the moiré lattices [1–3]. The latter is an interesting platform to investigate various strongly-correlated and frustration-induced phenomena, since the interaction parameters and carrier itineracy can be controlled by changing a twisted angle and the choice of two layers out of rich family of 2D materials [4–6]. Another useful platform to investigate the triangular lattice experimentally are the ultra-cold atomic gases on optical lattices [7–14]. The systems with triangular-lattice structure are found to host various phenomena, such as superconductivity [15–22], variety of charge and magnetic orderings [23–32], topological states [33, 34]. Among them, the charge ordering, e.g., (generalized) Wigner crystals [35–38], charge-transfer insulators, charge-density waves [39–42], or charge glasses attract researchers interest due to its interplay with superconductivity, as well as, possible applications in new devices, such as involving pyroelectric or ferroelectric materials [43]. Triangular lattices are commonly recognized to be perspective for searching the exotic charge orders, e.g., a pinball-liquid (PL) order [44–49]. The PL phase consists of the lattice sites that are insulating for the charge carriers (pins) but surrounded with the lattice sites where charge carriers are itinerant (balls), and thus the PL shares some properties of supersolids [50].

The model for the investigation of charge-ordering phenomenon is the extended Hubbard model (EHM) [51–59]. It has been investigated with the mean-field approximation (MFA) both in the context of organic conductors for the quarter-filling or 3/4-filling [60], and in the context of the moiré lattices for a series of a few fillings [37, 61, 62]. The methods beyond the MFA, such as the dynamical mean-field theory [63–65], are actively used to investigate the triangular-lattice materials with specific concentration of charge carriers as well [37, 46]. Nevertheless, to understand the full picture of various charge orders in the triangular lattice, the investigation in the grand-canonical ensemble with arbitrary charge concentration is required. The mean-field study of such a system can provide significant insights into the problem despite ignoring the correlation effects. Besides using it as a benchmark for further investigations, a number of unusual phenomena can already be found within the MFA, which makes them both easy to analyze and distinguish with strongly-correlated phenomena [66, 67]. The great advantage here (besides the required computational and time resources) is provided by the opportunity to analyze band structures. Moreover, the non-correlated phases are found within the dynamical mean-field theory when the intersite interaction prevails over the onsite interaction [68]. It is advantageous to use MFA results as a reference point in future studies together with the atomic limit results [69, 70].

Here, we present the solution of the triangular-lattice EHM within the MFA focusing on the zero-temperature systems without a magnetic order and utilizing the $\sqrt{3} \times \sqrt{3}$ hexagonal supercells. The found phase diagram consists of the large variety of phase transitions and is more

complex than one could assume in the absence of strong-correlation effects, which justified the use of MFA before taking them into account. Both the pinball-liquid phase and the (often ignored) strong particle-hole asymmetry are found and analyzed.

In the paper, after the discussion of the method of investigation (Sec. II), we present the known band structures of the non-interacting triangular and honeycomb lattices, required for the further discussion (Sec. III), and present the found mean-field phase diagram of the triangular lattice (Sec. IV) with a description of the found phases and phase transitions (Secs. IV A-IV C). Sec. IV E is devoted to the brief comparison of the mean-field and the atomic-limit results. The main finding are summarized in Sec. V.

II.   MODEL AND METHOD

The extended Hubbard model in a grand-canonical ensemble of electrons is represented by the Hamiltonian [51–59]:

$$\hat{H} = -t \sum_{\langle i,j\rangle,\sigma} \left(\hat{c}_{i\sigma}^\dagger \hat{c}_{j\sigma} + \text{H.c.}\right) + U \sum_i \hat{n}_{i\uparrow}\hat{n}_{i\downarrow} \quad (1)$$
$$+ \; V \sum_{\langle i,j\rangle} \hat{n}_i \hat{n}_j - \mu \hat{N},$$

where t, μ, U, and V are a hopping amplitude, a chemical potential, an onsite and an intersite nearest-neighbor (NN) interaction parameters, respectively. These parameters are effective, meaning they can include not only Coulomb repulsion but other interactions and renormalizations such as those that involve phonons. The i and σ are site and spin indices while the summation over $\langle i,j\rangle$ means a summation over NN pairs without repeating (i.e., if the term with ij is present in a sum, the term with ji is not). The $\hat{c}_{i\sigma}^\dagger$ and $\hat{c}_{i\sigma}$ are creation and annihilation operators, $\hat{n}_{i\sigma} = \hat{c}_{i\sigma}^\dagger \hat{c}_{i\sigma}$ is an occupation number operator, $\hat{n}_i = \hat{n}_{i\uparrow} + \hat{n}_{i\downarrow}$, and $\hat{N} = \sum_i \hat{n}_i$.

The mean-field approximation

$$\hat{n}_{i\sigma}\hat{n}_{j\sigma'} = n_{j\sigma'}\hat{n}_{i\sigma} + n_{i\sigma}\hat{n}_{j\sigma'} - n_{i\sigma}n_{j\sigma'} \quad (2)$$

($n_{i\sigma} = \langle\hat{n}_{i\sigma}\rangle$), and the Fourier transform to a reciprocal space turn the Hamiltonian into a sum of independent terms. In particular, for the triangular lattice and $\sqrt{3} \times \sqrt{3}$ supercell

$$\hat{H} = \sum_{\mathbf{k}\sigma} \left[\varepsilon_\mathbf{k}(\hat{c}_{1\mathbf{k}\sigma}^\dagger \hat{c}_{2\mathbf{k}\sigma} + \hat{c}_{3\mathbf{k}\sigma}^\dagger \hat{c}_{1\mathbf{k}\sigma} + \hat{c}_{2\mathbf{k}\sigma}^\dagger \hat{c}_{3\mathbf{k}\sigma}) + \text{H.c.}+\right.$$
$$\left. + \sum_\alpha \epsilon_{\alpha\sigma}\hat{n}_{\alpha\mathbf{k}\sigma}\right] + C = \sum_{\mathbf{k}\sigma} \hat{H}_{\mathbf{k}\sigma} + C, \quad (3)$$

where $\alpha = 1, 2, 3$ is a sublattice index, $\mathbf{k}$ is a reciprocal-space vector, the constant term

$$C = -\frac{L}{3} \sum_\alpha \left(U n_{\alpha\uparrow}n_{\alpha\downarrow} + \frac{zV}{2} n_{\bar\alpha}n_{\bar{\bar\alpha}}\right), \quad (4)$$

($\bar\alpha$ and $\bar{\bar\alpha}$ are sublattice indices different from α and from each other), L is the number of lattice sites, $n_\alpha = \frac{3}{L} \sum_{\sigma\mathbf{k}} \langle\hat{n}_{\alpha\mathbf{k}\sigma}\rangle$, $z = 6$ is a coordination number,

$$\epsilon_{\alpha\sigma} = U n_{\alpha\bar\sigma} + \frac{zV}{2}(n_{\bar\alpha} + n_{\bar{\bar\alpha}}), \quad (5)$$

($\bar\sigma$ is the spin index different from σ) and

$$\varepsilon_\mathbf{k} = -t\left(e^{i\mathbf{k}\mathbf{r}_1} + e^{i\mathbf{k}\mathbf{r}_2} + e^{i\mathbf{k}\mathbf{r}_3}\right) \quad (6)$$

with:

$$\mathbf{r}_1 = \left(-\frac{1}{3}, -\frac{2}{3}\right), \; \mathbf{r}_2 = \left(-\frac{1}{3}, \frac{1}{3}\right), \; \mathbf{r}_3 = \left(\frac{2}{3}, \frac{1}{3}\right), \quad (7)$$

provided that the vectors $\mathbf{k}$ are written in the basis of a cell that is reciprocal to the $\sqrt{3} \times \sqrt{3}$ supercell.

Each term in the Hamiltonian (3) can be written in a block-diagonal matrix form:

$$\hat{H}_{\mathbf{k}\sigma} = \begin{pmatrix} 0 & \mathbf{0}_{1\times 3} & \mathbf{0}_{1\times 3} & 0 \\ \mathbf{0}_{3\times 1} & \mathbf{H}_{1\mathbf{k}\sigma} & \mathbf{0}_{3\times 3} & \mathbf{0}_{3\times 1} \\ \mathbf{0}_{3\times 1} & \mathbf{0}_{3\times 3} & \mathbf{H}_{2\mathbf{k}\sigma} & \mathbf{0}_{3\times 1} \\ 0 & \mathbf{0}_{1\times 3} & \mathbf{0}_{1\times 3} & \epsilon_1 + \epsilon_2 + \epsilon_3 \end{pmatrix}_{\mathbf{k}\sigma}, \quad (8)$$

where $\mathbf{0}_{m\times n}$ denotes a block of $m \times n$ size with all elements 0, whereas blocks $\mathbf{H}_{1\mathbf{k}\sigma}$ and $\mathbf{H}_{2\mathbf{k}\sigma}$ are defined as

$$\mathbf{H}_{1\mathbf{k}\sigma} \equiv \begin{pmatrix} \epsilon_{1\sigma} & \varepsilon_\mathbf{k} & \varepsilon_\mathbf{k}^* \\ \varepsilon_\mathbf{k}^* & \epsilon_{2\sigma} & \varepsilon_\mathbf{k} \\ \varepsilon_\mathbf{k} & \varepsilon_\mathbf{k}^* & \epsilon_{3\sigma} \end{pmatrix}, \quad (9)$$

and

$$\mathbf{H}_{2\mathbf{k}\sigma} \equiv \begin{pmatrix} \epsilon_{1\sigma} + \epsilon_{2\sigma} & \varepsilon_\mathbf{k} & -\varepsilon_\mathbf{k}^* \\ \varepsilon_\mathbf{k}^* & \epsilon_{1\sigma} + \epsilon_{3\sigma} & \varepsilon_\mathbf{k} \\ \varepsilon_\mathbf{k} & \varepsilon_\mathbf{k}^* & \epsilon_{2\sigma} + \epsilon_{3\sigma} \end{pmatrix}. \quad (10)$$

The subscript $\mathbf{k}\sigma$ in Eq. (8) means that the operator acts only in a space formed by basis functions

$$|0_{1\mathbf{k}\sigma}0_{2\mathbf{k}\sigma}0_{3\mathbf{k}\sigma}\rangle,$$
$$|1_{1\mathbf{k}\sigma}0_{2\mathbf{k}\sigma}0_{3\mathbf{k}\sigma}\rangle, \quad |0_{1\mathbf{k}\sigma}1_{2\mathbf{k}\sigma}0_{3\mathbf{k}\sigma}\rangle, \quad |0_{1\mathbf{k}\sigma}0_{2\mathbf{k}\sigma}1_{3\mathbf{k}\sigma}\rangle,$$
$$|1_{1\mathbf{k}\sigma}1_{2\mathbf{k}\sigma}0_{3\mathbf{k}\sigma}\rangle, \quad |1_{1\mathbf{k}\sigma}0_{2\mathbf{k}\sigma}1_{3\mathbf{k}\sigma}\rangle, \quad |0_{1\mathbf{k}\sigma}1_{2\mathbf{k}\sigma}1_{3\mathbf{k}\sigma}\rangle,$$
$$|1_{1\mathbf{k}\sigma}1_{2\mathbf{k}\sigma}1_{3\mathbf{k}\sigma}\rangle. \quad (11)$$

Thus, the model can be easily solved on a fine grid of $\mathbf{k}$-vectors when the parameters V/t, U/t, μ/t, and $n_{\alpha\sigma}$ are provided. To distinguish stable and metastable phases the grand potential is calculated as

$$\frac{\Omega}{L} = \frac{1}{L}\left(C - \frac{1}{\beta}\ln\mathcal{Z}\right) = \frac{1}{L}\left(C - \frac{1}{\beta}\sum_{\mathbf{k}\sigma}\ln\mathcal{Z}_{\mathbf{k}\sigma}\right), \quad (12)$$

where $\mathcal{Z} = \prod_{\mathbf{k}\sigma} \mathcal{Z}_{\mathbf{k}\sigma}$ is the partition function of the system, $\mathcal{Z}_{\mathbf{k}\sigma} = \sum_m e^{-\beta E_{\mathbf{k}\sigma}^{(m)}}$, $E_{\mathbf{k}\sigma}^{(m)}$ is the mth eigenvalue of $\hat{H}_{\mathbf{k}\sigma}$ (i.e., of the matrix (8)), and $\beta = T^{-1}$ is the inverse temperature.

The solution of the model gives the occupation numbers:

$$n_{\alpha\sigma} = \frac{3}{L} \sum_{\mathbf{k}} \frac{\sum_m n_{\alpha\mathbf{k}\sigma}^{(m)} e^{-\beta E_{\mathbf{k}\sigma}^{(m)}}}{\mathcal{Z}_{\mathbf{k}\sigma}}, \qquad (13)$$

where

$$\begin{aligned}
n_{\alpha\mathbf{k}\sigma}^{(m)} &= \left| a_{\alpha\mathbf{k}\sigma}^{(m)} \right|^2 + \left| a_{\alpha\mathbf{k}\sigma,\bar{\alpha}\mathbf{k}\sigma}^{(m)} \right|^2 \\
&+ \left| a_{\alpha\mathbf{k}\sigma,\bar{\bar{\alpha}}\mathbf{k}\sigma}^{(m)} \right|^2 + \left| a_{1\mathbf{k}\sigma,2\mathbf{k}\sigma,3\mathbf{k}\sigma}^{(m)} \right|^2,
\end{aligned} \qquad (14)$$

and $a^{(m)}$ are components of the mth eigenvector of the matrix (8).

In this research, we focus on the charge-order phenomenon neglecting possible spin-order formation. Hence, the equations are simplified such that $n_{\alpha\sigma} = n_\alpha/2$ and $\epsilon_\alpha \equiv \epsilon_{\alpha\sigma}$.

Since the n_α take role of both input and output quantities of the model, it can be solved self-consistently. In this research, our point of interest is the zero-temperature phase diagram. However, due to the lack of convergence, the calculations are performed for $T = 10^{-3} \cdot 4.5t$ which stabilizes the algorithm. Still, rather strong mixing is used: when the Fermi level is in a proximity of a singularity of a spectral function, only $0.005 - 0.07$ fraction of a new solution is used for the next iteration. A strict criterion of convergence is used: 10^{-8} for n_α together with $10^{-8} \cdot 4.5t$ for Ω/L. The grid of $\mathbf{k}$-points contained 96×96 points (817 irreducible points; the $\mathbf{k}$-dependent quantities exhibit the symmetry of the non-symmetry-broken triangular lattice (wallpaper group p6m), despite the fact the the supercell has a lower symmetry (p3m1)).

For the sake of better comparison with other lattice models, the quantities are expressed in the units of a half-bandwidth of a non-interacting triangular lattice $D = 4.5t$. For the same reason, the intersite interaction V is expressed in the units of $D/z = 0.75t$. In the plots, the displaced chemical potential $\bar{\mu} = \mu - U/2 - zV$ is used.

We denote the total concentration $n = \sum_\alpha n_\alpha/3$. For the analysis of discontinuous phase transitions, the contributions to the grand potential Ω (all per lattice site L) are defined as the thermal averages of the corresponding terms in the Hamiltonian (1): kinetic energy (t-term contribution), on-site interaction energy (U-term contribution), intersite-interaction energy (V-term contribution), potential energy (V- and U-term contributions together), and chemical energy (μ-term contribution). At finite temperatures Ω also has a contribution $-TS$ (S is an entropy of the system) which is zero in this research.

One of the advantages of MFA is the ability to plot and analyze a band structure $\omega(\mathbf{k})$. It is found as eigenvalues of a matrix:

$$\begin{pmatrix} \epsilon_1 & \varepsilon_{\mathbf{k}} & \varepsilon_{\mathbf{k}}^* \\ \varepsilon_{\mathbf{k}}^* & \epsilon_2 & \varepsilon_{\mathbf{k}} \\ \varepsilon_{\mathbf{k}} & \varepsilon_{\mathbf{k}}^* & \epsilon_3 \end{pmatrix}. \qquad (15)$$

The spectral function is calculated as

$$A_\alpha(\omega + i\eta) = -\frac{1}{\pi} \frac{3}{L} \sum_{\mathbf{k}} \operatorname{Im} G_{\alpha\alpha\mathbf{k}}(\omega + i\eta), \qquad (16)$$

where $\eta = 0.001D - 0.005D$, and $G_{\alpha\alpha\mathbf{k}}(z)$ are diagonal elements of a matrix

$$\begin{pmatrix} z - \epsilon_1 & -\varepsilon_{\mathbf{k}} & -\varepsilon_{\mathbf{k}}^* \\ -\varepsilon_{\mathbf{k}}^* & z - \epsilon_2 & -\varepsilon_{\mathbf{k}} \\ -\varepsilon_{\mathbf{k}} & -\varepsilon_{\mathbf{k}}^* & z - \epsilon_3 \end{pmatrix}^{-1}. \qquad (17)$$

When the spectral function is calculated with such a small η, the grid of 396×396 $\mathbf{k}$-points or more is used to make plots of spectral function clear.

The calculations are implemented in the Python language with the use of Matplotlib library for visualization.

III. NON-INTERACTING LIMIT

For the reference point and the following analysis, the band structures and the densities of states (DOSs) of non-interacting triangular and honeycomb lattices are presented in Fig. 1. Both the no-sublattice case (Fig. 1a) and the 3-sublattice case with the bands folded in accordance with $\sqrt{3} \times \sqrt{3}$ supercell (Fig. 1b) are shown.

The DOS (per spin) of a triangular lattice is [71]:

$$\rho_{\text{tri}}(\omega) = \frac{K(z_1/z_0)}{\pi^2 t \sqrt{z_0}}, \qquad (18)$$

where: $K(m)$ is the complete elliptic integral of the first kind,

$$K(m) = \int_0^{\frac{\pi}{2}} \frac{d\theta}{\sqrt{1 - m\sin^2\theta}}, \qquad (19)$$

$$z_0 = \begin{cases} 3 + 2\sqrt{3 - \omega/t} - \left(\frac{\omega/t}{2}\right)^2, & \text{for } 2 \le \omega/t \le 3 \\ 4\sqrt{3 - \omega/t}, & \text{for } -6 \le \omega/t \le 2 \end{cases},$$

$$z_1 = \begin{cases} 4\sqrt{3 - \omega/t}, & \text{for } 2 \le \omega/t \le 3 \\ 3 + 2\sqrt{3 - \omega/t} - \left(\frac{\omega/t}{2}\right)^2, & \text{for } -6 \le \omega/t \le 2 \end{cases}.$$

It is asymmetric, exists from $-6t$ to $3t$, and has a van Hove singularity at $2t$. The zero-temperature half-filling would correspond to a Fermi level $\omega_{\text{F}} \approx 0.8347t$.

The DOS (per spin) of a honeycomb lattice is [72, 73]:

$$\rho_{\text{hcb}}(\omega) = 2|\omega|\rho_{\text{tri}}(3 - \omega^2). \qquad (20)$$

It is symmetric around the Dirac cone at $\omega = 0t$, exists from $-3t$ to $3t$, and has van Hove singularities at $\pm t$ (Fig. 1c).

IV. PHASE DIAGRAM

The phase diagram is shown in Fig. 2 while the structures of the found charge orders are schematically presented in Fig. 3. In the model (1), the lattice is fully
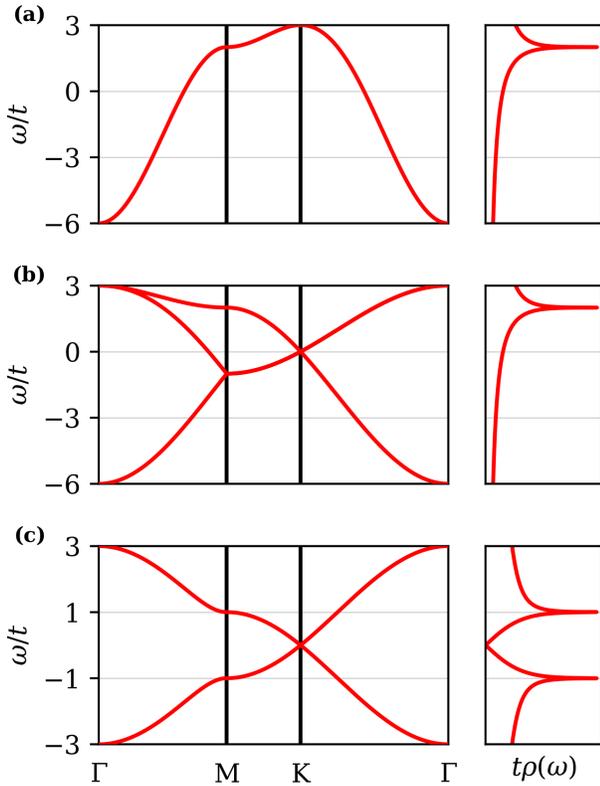
FIG. 1. The non-interacting band structures (left) and densities of states (right) of (a) triangular, (b) triangular with the $\sqrt{3} \times \sqrt{3}$ supercell, and (c) honeycomb lattices.

FIG. 2. The MFA phase diagram of the triangular-lattice EHM with 3-sublattices as a function of V and $\bar{\mu} = \mu - U/2 - zV$ for $U = 0D$ and $U = 2D$. Only the phases with the smallest grand potential are shown. The subscripts in the phase names refer to the charge order (see Fig. 3) while letters M and I stand for the metallic and insulating phase, respectively. The solid and dashed lines represent continuous and discontinuous phase transitions, respectively. The dotted line is placed at the approximate transition where the charge-ordered metal is not a pinball liquid (PL) anymore. The total concentration is constant along the green dashed lines, in particular $n = 1/3$, $2/3$, 1, $4/3$, and $5/3$ (from left to right).

unoccupied (I_{000}) for $\bar{\mu} < -(zV + U/2 + 6t)$ and fully occupied (I_{222}) for $\bar{\mu} > zV + U/2 + 3t$. The corresponding regions on the phase diagrams are indicated by gray color in Fig. 2.

The metallic phase without charge order (CO) is denoted as M_{AAA} or as the Fermi liquid (FL) and marked by the red color. Its band structure and spectral function fully repeat the non-interacting ones (Fig. 1b) except the Fermi level is shifted by:

$$\omega_{\text{shift}} = \left(zV + \frac{U}{2} \right) (n - 1) - \bar{\mu}, \qquad (21)$$

(cf. Eq. (5) when all $n_{\alpha\sigma}$ are equal). It is possible to have convergence of an algorithm for the non-charge-ordered phase throughout the whole phase diagram. However, the further it goes into the charge-ordered regions of the phase diagram, the easier it can be destabilized toward CO phases by introduction of small deviations in the input n_{α}, and the larger the difference between its grand potential and the grand potential of the CO phases.

The blue and yellow regions of the phase diagram in Fig. 2 mark the CO phases with the sublattice occupation numbers $n_1 = n_A$, $n_2 = n_3 = n_B$ (ABB phases, Fig. 3c) and $n_1 = n_2 = n_A$, $n_3 = n_B$ (AAB phases, Fig. 3d),

respectively, with $n_A > n_B$. These phases have degeneracy of 3, e.g., the possible sublattice occupation numbers n_{α} of the yellow region (AAB region) are (n_A, n_A, n_B), (n_A, n_B, n_A), and (n_B, n_A, n_A).

The yellow region (subsection IV A) encompasses two CO metallic phases (M^1_{AAB} and M^2_{AAB}) and an insulating one (I_{AAB}). The total concentration in the latter is always $4/3$, while in the atomic-limit case it has the sublattice occupation numbers $(2, 2, 0)$. The M^1_{AAB} phase is in fact a so-called pinball liquid (PL) phase, i.e. the electrons cannot hop through one of the sublattices which takes role of pins, while the honeycomb lattice formed by the other two sublattices is metallic. The phase loses its PL properties as it approaches a FL phase (the dotted line).

The blue region in Fig. 2 (subsection IV B) encompasses two CO metallic phases (M^1_{ABB} and M^2_{ABB}) and
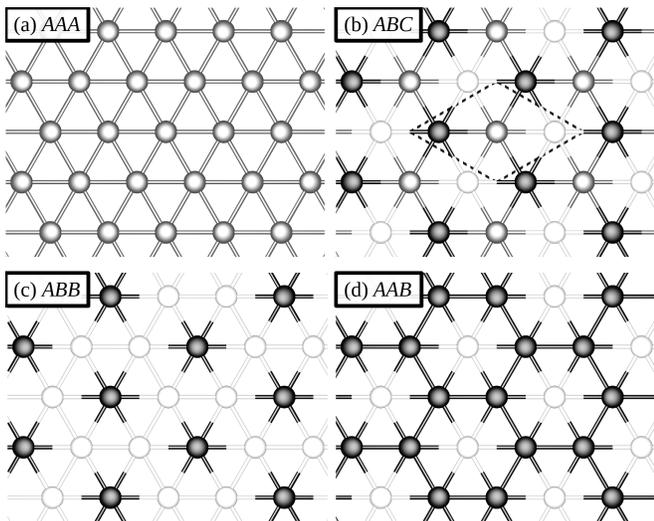
FIG. 3. The found charge order types on the triangular lattice. The color of the circles represent the relative charge concentration on the lattice sites: from the highest (black circles) to the lowest (white circles). The $\sqrt{3} \times \sqrt{3}$ supercell is shown by the dashed lines. The figure is prepared using VESTA PROGRAM [74].

FIG. 4. The order parameters in the AAB region (left) and representative band structures of the AAB phases (right). The vertical dashed lines show the locations of phase transitions.

an insulating one (I_{ABB}, $n = 2/3$) which in the atomic-limit case has the sublattice occupation numbers $(2, 0, 0)$.

When $U > 0D$, CO metallic phases with the most broken symmetry occur, i.e., all three occupation numbers in the sublattices are different from each other (M_{ABC}, white region, Fig. 3b, subsection IV D). The two phases can be identified in this region: an ABB-like M_{ABC} phase and an AAB-like M_{ABC} phase. The degeneracy of the phases is 6.

A. AAB Region

Two continuous phase transitions and the band structures of the AAB phases (yellow-region phases in Fig. 2) are shown in Fig. 4. For the whole band-structure evolution between $\bar{\mu} = 1.50D$ and $\bar{\mu} = 2.60D$ for $U = 2.00D$ and $zV = 3.50D$ see the file M1_U2.00_V3.50_AAB.mp4 [75]. Since sublattices in this region are occupied by two different occupation numbers only, the useful order parameter is a polarization

$$\Delta = \frac{n_A - n_B}{2}. \qquad (22)$$

The spectral weight $A_A(\omega) = 2A_1(\omega) = 2A_2(\omega)$ and $A_B(\omega) = A_3(\omega)$.

When not in the proximity of the FL or I_{222} phases (see subsection IV C), the AAB phases can be described as a separate triangular lattice formed by the sublattice with the occupation n_B (triangular-B lattice), a honeycomb lattice represented by the sublattices with the occupation n_A (honeycomb-A lattice), and a certain amount of hybridization between them (cf. the non-interacting band

structures in Fig. 1a and 1c). The hopping between sites of the triangular-B lattice takes place by means of this hybridization with the honeycomb-A lattice and hance has a modified amplitude: the opposite sign and a smaller absolute value. As the intersite interaction V increases, the hybridization decreases. This turns the triangular-like band into a dispersionless atomic level, while the lower bands become indistinguishable from the non-interacting honeycomb band structure (Fig. 1c) with a shifted Fermi level. For a band-structure evolution with the increase of V see the file M2_U2.00_mu2.00_AAB.mp4 [75]. The above is valid for all AAB phases.

Noticeably, a position of a Dirac cone at the K-point of the honeycomb-like bands and a position of an extremum at the K-point of the triangular-like band are always fixed at

$$\omega_A = \omega_{\text{shift}} - \frac{\omega_\Delta}{3}, \qquad \omega_B = \omega_{\text{shift}} + \frac{2\omega_\Delta}{3}, \qquad (23)$$

respectively, where the distance between them:

$$\omega_\Delta = (zV - U)\Delta. \qquad (24)$$

The other way to write these expressions is

$$\omega_\alpha = \omega_{\text{shift}} + (zV - U)\frac{n - n_\alpha}{2} \qquad (25)$$

(in this subsection, $\omega_A = \omega_1 = \omega_2$ and $\omega_B = \omega_3$).

To get more insights on AAB phases, the lower bands (honeycomb-like bands) are shown in Fig. 5 together with $\pm 3t$ and $\pm t$ lines where the non-interacting honeycomb band structure has edges and van Hove singularities. It turns out that the upper edge and the lower

singularity are always fixed at $\omega_A + 3t$ and $\omega_A - t$, respectively. It justifies the lack of dependency on the interaction V of a left boundary of the I_{AAB} phase in Fig. 2. Consequently, the band gap of the I_{AAB} phase:

$$\omega_{\text{gap}} = \omega_\Delta - 3t = (zV - U)\Delta - 3t \qquad (26)$$

(asymptotically approaches $zV - U - 3t$ for a large V).
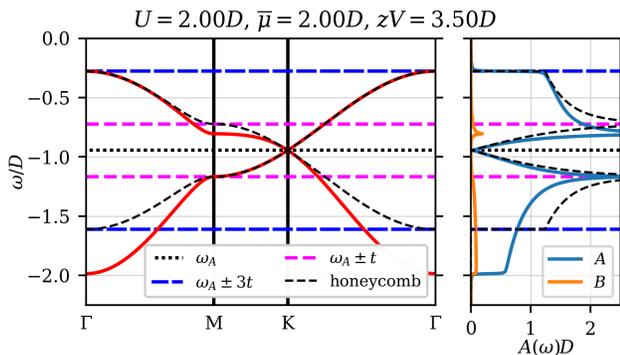
FIG. 5. Comparison between the lower bands of an AAB-region phase (solid lines) and the non-interacting honeycomb bands (shifted to ω_A).

On the energy scale the hybridization with the triangular-B lattice is concentrated around the lower edge and the upper singularity of the honeycomb-like bands. It is clear from the non-zero spectral weight of the triangular-B lattice. Locations of these points are not fixed to $-3t$ and t, but approach these values in the large-V limit where the hybridization disappears (see the file `M2_U2.00_mu2.00_AAB.mp4` [75]).

Since there is no spectral weight of the triangular-B lattice close to the maximum of the lower bands, the M^1_{ABC} phase is a *pinball liquid*. Close to the FL phase, the upper and lower bands start to merge and the phase is not a PL anymore. This transition is continuous and very smooth (see for example Fig. S1d and S1e [75]). To give an approximate boundary of the PL phase, the dotted line in Fig. 2 shows the points where the maximum of the lower bands (located at the Γ-point) and the minimum of the upper band (located at the K-point) have the same energy. From the expressions above it is clear that this line exactly corresponds to $\omega_\Delta = 3t$.

For $U = 0D$ or close to $0D$, the I_{AAB}-M^2_{AAB} transition is sharp and gets discontinuous for $\bar{\mu} \gtrsim 3D$ (see for example Fig. S2a [75]). It can be justified by the proximity of the transition to the fully occupied phase (I_{222}). The total concentration in I_{AAB} and I_{222} phases is always $4/3$ and 2, respectively, while the transition between M^2_{AAB} and I_{222} phases is continuous (subsection IV C). As a consequence the sharp change in occupation numbers occurs at the I_{AAB}-M^2_{AAB} transition. When moving from the CO metallic phase, this discontinuous transition corresponds to the release of the potential energy at the expense of the chemical energy.

It is worth noting, since the M^2_{AAB} phase exists for any large values of V (when $\bar{\mu}$ is also large), and in the large-V limit the hybridization between the honeycomb-A and the triangular-B lattices disappears, it eventually becomes an insulator: the Fermi level is located in the atomic-like peak formed by the sublattice with the occupation n_B (and both n and n_B are not integer!), while the hopping with neighboring sites is restricted. This situation is rather unphysical, and both an inclusion of a next-nearest-neighbor hopping, and an inclusion of the Mott physics can resolve it.

B. *ABB* Region

The band structures of the ABB phases (blue region in Fig. 2) and phase transitions between them are shown in Fig. 6. For the whole band structure evolution during these transitions see also the file `M3_U2.00_V3.50_ABB.mp4` [75]. Here, the spectral weight $A_A(\omega) = A_1(\omega)$ and $A_B(\omega) = 2A_2(\omega) = 2A_3(\omega)$.
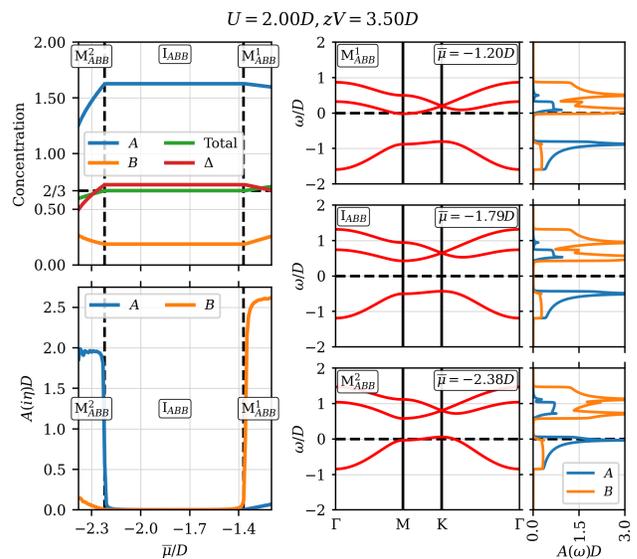
FIG. 6. The order parameters in the ABB region (left) and representative band structures the ABB phases (right). The vertical dashed lines show the locations of phase transitions.

In the ABB region, honeycomb-like bands of a lattice formed by the sublattices with the occupation n_B (honeycomb-B lattice) are located above a triangular-like band of a lattice formed by the sublattice with the occupation n_A (triangular-A). It is clear, that the upper bands look less like the honeycomb bands (Fig. 1c) for $zV = 3.50D$ in comparison to the AAB lower bands for the same V. It is justified by the fact that the 1st and the 2nd bands in Fig. 1b can be transformed to the honeycomb bands (Fig. 1c) with less effort than the 2nd and the 3rd bands. When V increases, the bands change accordingly to form non-interacting honeycomb-like and

triangular-like (eventually, an atomic-like) bands while the hybridization between them disappears: see the file `M4_U2.00_mu-1.80_ABB.mp4` [75].

Positions of the K-point extremum of the triangular-like band and the Dirac cone of the honeycomb-like bands are still fixed to the energies defined by Eq. (25) ($\omega_A = \omega_1$ and $\omega_B = \omega_2 = \omega_3$) or, in terms of the polarization,

$$\omega_A = \omega_{\text{shift}} - \frac{2\omega_\Delta}{3}, \qquad \omega_B = \omega_{\text{shift}} + \frac{\omega_\Delta}{3}. \qquad (27)$$

Similar to the AAB phases, the upper edge and the lower singularity of the honeycomb-like bands are also fixed to $3t$ and $-t$ in contrast to the lower edge and the upper singularity that approach $-3t$ and t only in the large-V limit when the hybridization disappears. Since, the lower edge is now adjacent to a band gap, the ABB phases are noticeably different from the AAB phases. The right boundary of the I_{ABB} phase in Fig. 2 is dependent on V. The expression of the lower limit only of the I_{ABB}-phase band gap can be written:

$$\omega_{\text{gap}} \geq (zV - U)\Delta - 3t. \qquad (28)$$

When V increases, the ω_{gap} asymptotically approaches the right-side expression.

Since the hybridization between the honeycomb-B and triangular-A lattices is concentrated around the minimum of the honeycomb-like bands, exactly where the Fermi level of the M^1_{ABB} phase is located, the phase is not a PL. In the limit of large V the hybridization disappears; hence, in this limit, the M^1_{ABB} phase would eventually become a PL, but the border of such a transition is vague. Similarly to the M^2_{AAB}, the M^2_{ABB} phase in large-V limit is an insulator with non-integer occupations which can be viewed as an artifact of a model or its mean-field treating.

In contrast to the AAB region, the M^2_{ABB} phase does not exist for $U = 0D$ or close to $0D$. The discontinuous transition to the FL phase (subsection IV C) takes place directly from I_{ABB} phase.

C. Symmetry Breaking from a Non-Charge-Ordered Phase

Throughout most of the range of μ the transitions from the FL phase (M_{AAA}, red region in Fig. 2) to the CO phases (M^1_{ABB}, M^2_{ABB}, I_{ABB}, M^1_{AAB}, M^2_{AAB}, I_{AAB}) are discontinuous (see for example Fig. S1 [75]). Noticeably, these transitions take place for $zV \gtrsim U + D$. The discontinuous symmetry breaking corresponds to the release of intersite-interaction energy at the expense of both kinetic and on-site-interaction energy. Additionally, the chemical energy decreases with transitions to the M^2_{ABB} and I_{ABB} phases, and increases with transitions to the M^2_{AAB} and I_{ABB} phases. The CO phases are metastable inside the FL region for a rather small range of parameters: on the zV axis the span of this range is up to $0.1D$

for the most noticeable hysteresis (I_{ABB}-M_{AAA} transition for $U = 0D$ and large hole doping).

The analysis of band structures shows that the CO phases get unstable when the Fermi level approaches certain valleys or saddle points. Moreover, there are ranges of μ where the symmetry-breaking transitions to the CO metallic phases are continuous (see continuous evolutions in the files `M*_SymBreak.mp4` [75]).

1. M^1_{ABB} and I_{ABB} Phases

The CO M^1_{ABB} and I_{ABB} phases become unstable when the Fermi level approaches (from above) the maximum of the lower (triangular-like) band located at the K-point (see their phase diagrams in Fig. 6 for the reference).

For the continuous transition to the FL, the maximum of the triangular-like band should merge with the Dirac point of the honeycomb-like bands at the K-point. The Fermi level cannot be above the Dirac point because it destabilizes the M^1_{ABB} phase towards an AAB phase. However, the Fermi level stays between the maximum of the triangular-like band and the Dirac point close to the triple phase-transition point of the M_{AAA}, M^1_{ABB}, and M^1_{AAB} phases. There, the continuous symmetry breaking to the M^1_{ABB} phase takes place. It is visualized in the file `M5_U2.00_mu-0.85_ABB_SymBreak.mp4` [75].

Since the Fermi level appears where all three bands of the FL phase are degenerate at the K-point, the $\omega_{\text{shift}} = 0t$ around the continuous transition, i.e.

$$\bar{\mu} = \left(zV + \frac{U}{2}\right)(n - 1), \qquad (29)$$

where $n \approx 0.7973$ is the non-interacting triangular-lattice occupation that corresponds to $\omega_F = 0t$. Noticeably, around the triple point the $zV \approx U + D$ which brings us to the expression:

$$\frac{\bar{\mu}}{D} \approx 0.10 - 0.30\frac{zV}{D} \qquad (30)$$

for the triple point.

2. M^1_{AAB} Phase

Similarly, the M^1_{AAB} phase (but not I_{AAB}) becomes unstable towards the FL phase when the Fermi level approaches (from below) the minimum of the upper (triangular-like) band at the K-point (see its phase diagram in Fig. 4 for the reference). The same as for the M^1_{ABB} phase, the continuous phase transition (merging the extremum of the triangular-like band and the Dirac point at the K-point) happens around the same triple point of the phase diagram where Eq. (29) is satisfied with the same n. The continuous transition is visualized in the file `M6_U2.00_mu-0.80_AAB_SymBreak.mp4` [75].

3. M_{ABB}^2 Phase

For U close to $0D$, there is no transition between the FL phase and the M_{ABB}^2 phase. For a larger U, the CO phase becomes unstable towards the FL phase in two ways: 1) when the Fermi level approaches (from above) the singularity (saddle point) of the lower (triangular-like) band at the M-point; 2) when the Fermi level approaches (from below) the minimum of the upper (honeycomb-like) bands which in this range of parameters is at the M-point.

The continuous transition between the FL and M_{ABB}^2 phase happens in the small range of μ when the Fermi level stays in between of the mentioned saddle point and minimum at the M-point. It is visualized in the file `M7_U2.00_mu-1.80_ABB_SymBreak.mp4` [75]. Since the Fermi level appears where the two bands of the FL phase are degenerate at the M-point, the $\omega_{\text{shift}} = t$ around the continuous transition, i.e.

$$\bar{\mu} + t = \left(zV + \frac{U}{2}\right)(n-1), \qquad (31)$$

where $n \approx 0.6078$ is the non-interacting triangular-lattice occupation when $\omega_{\text{F}} = -t$.

4. M_{AAB}^2 and I_{AAB} Phases

The M_{AAB}^2 and I_{AAB} phases become unstable towards the FL phase when the Fermi level approaches (from above) the maximum of the lower (honeycomb-like) bands at the Γ-point.

In contrast to the M_{ABB}^2, the M_{AAB}^2 phase cannot continuously transform to the FL but has an infinite range of μ (particularly, $\bar{\mu} \gtrsim 3(U/2 + D)$) where it continuously transforms to the fully occupied phase (I_{222}). The continuous transition is visualized in the file `M8_U0.00_mu3.10_AAB_SymBreak.mp4` [75].

At this continuous transition the $\omega_{\text{shift}} = -3t$ with $n = 2$ which corresponds to the top of the non-interacting triangular-lattice bands:

$$\bar{\mu} - 3t = zV + \frac{U}{2}. \qquad (32)$$

D. AAB-ABB Transition and ABC Region

The transition between the M_{ABB}^1 and M_{AAB}^1 phases (between the yellow and blue regions) is discontinuous (see for example Fig. S2a [75]). When moving from the ABB phase, it happens with the release of chemical energy at the expense of intersite-interaction energy.

For $U > 0D$ an intermediate region of M_{ABC} phases ($n_1 = n_A$, $n_2 = n_B$, $n_3 = n_C$, $n_A > n_B > n_C$, white region) opens between the ABB and AAB regions (see for example Fig. S3d [75]). For the most range of parameters the transition between the ABC region and the M_{ABB}^1

phase on one side and the M_{AAB}^1 phase on the other side is continuous. Note that the less-symmetry-broken phases (ABB and AAB) can have the self-consistent solution of the Hamiltonian (3) inside the ABC region despite other indicators that the phase transition is continuous.

The ABC region can be characterized by identifying two phases: the ABB-like M_{ABC} phase and the AAB-like M_{ABC} phase with the discontinuous transition between them. Moreover, there is a range of V where the AAB-like M_{ABC} phase discontinuously transforms directly into the M_{ABB}^1 phase (see Fig. 2). The same as for the M_{ABB}^1-M_{AAB}^1 transition, these discontinuous transitions take place with the release of chemical energy at the expense of intersite-interaction energy when moving from the ABB-like side.

There is a range of parameters where the ABC phase can be viewed as both ABB-like and AAB-like M_{ABC} phase (in Fig. 2 the region around $zV = 4.4D$ for $U = 2D$). The visualization of two continuous transitions between the ABB, ABC, and AAB regions for $U = 2D$ and $V = 4.4D$ is presented in the file `M9_U2.00_V4.40 _ABB-ABC-AAB.mp4` [75].

The band structure of the M_{ABC} phase consists of 3 bands: a lower triangular-like which spectral weight primarily comes from the A-sublattice, an upper triangular-like which spectral weight primarily comes from the C-sublattice, and an intermediate band which spectral weight primarily comes from the B-sublattice. The Fermi level is located inside the intermediate band. All three bands have an extremum at the K-point that is fixed to the energy defined from Eq. (25) ($\omega_A = \omega_1$, $\omega_B = \omega_2$, and $\omega_C = \omega_3$). In the large-V limit the three bands are rather three atomic levels: a fully occupied level, a fully unoccupied level, and a level where the Fermi level is located.

E. Correspondence to the Atomic-Limit Phase Diagram

For a large V the atomic-limit solution of the triangular-lattice EHM predicts 7 phases that are denoted according to the three occupation numbers: 000, 100, 200, 210, 220, 221, and 222 [69]. The phase transitions take place at the following lines:

$$\begin{aligned}
\bar{\mu} &= \mp(zV + U/2), &&\text{for 000-100 and 222-221,}\\
\bar{\mu} &= \mp(zV - U/2), &&\text{for 100-200 and 221-220,} \quad (33)\\
\bar{\mu} &= \mp U/2, &&\text{for 200-210 and 220-210,}
\end{aligned}$$

where the '$\mp$' corresponds to the first or second boundary mentioned above, respectively. It is clear from the formulas that the phases 100, 210 and 221 do not exist for $U = 0D$.

There is a correspondence between the atomic-limit and mean-field solutions at a large V. Besides the obvious correspondence for the fully-unoccupied and fully-

occupied phases, the atomic-limit 100 phase can be associated with the mean-field M^2_{ABB} phase, the 200 phase with the I_{ABB} and M^1_{ABB} phases together, the 210 phase with M_{ABC} phase, and correspondingly for the other side of the phase diagram.

Thus, the disappearance of the M_{ABC} and M^2_{ABB} phases for $U = 0D$ could be predicted from the atomic-limit solution. Despite this correspondence, the mean-field phase M^2_{AAB} exists even for $U = 0D$ and large V, which makes it an unexpected effect of non-zero itinerancy.

To compare the atomic-limit and the mean-field solutions, one can put $U = 2D$ in Eqs. (33) (despite the fact that $D = 0$ in the atomic limit):

$$\bar{\mu} = \mp(zV + D), \text{ for 000-100 ('−') and 222-221 ('+'),}$$
$$\bar{\mu} = \mp(zV - D), \text{ for 100-200 ('−') and 221-220 ('+'),}$$
$$\bar{\mu} = \mp D, \qquad \text{ for 200-210 ('−') and 220-210 ('+').}$$

The mean-field boundaries of M_{ABC} phase at large V and $U = 2D$ indeed slowly approach $\bar{\mu} = \mp D$ (Fig. 2). The same is valid for the boundaries of the I_{000} and I_{222} phases since the terms $-6t$ and $3t$ become negligible in comparison to the large zV. The left boundary of the I_{ABB} phase coincide well with the left boundary of the atomic-limit 200 phase even at the small values of V, and the same is valid for the 220 and I_{AAB} phases.

It is reasonable to expect that primarily those phases that are associated with non-zero U (M_{ABC}, M^2_{ABB}, M^2_{AAB}) will be modified when taking into account the Mott physics (local correlations). Note also, that in the atomic limit there are also 111 (Mott insulator), 110, and 211 phases for small V (particularly, for $zV \leq 2U$).

V. SUMMARY

The full zero-temperature phase diagram of the extended Hubbard model on the triangular lattice in the all-encompassing range of chemical potential values and repulsive onsite and nearest-neighbor electron interactions is presented and analyzed. Despite the limitations of the mean-field approximation, restriction to the $\sqrt{3} \times \sqrt{3}$ supercells and the absence of magnetic order, the large variety of features are found. Those are the diverse and numerous phase transitions, including the continuous and discontinuous symmetry breakings; the pinball liquid phase; the strong particle-hole asymmetry manifested in every phase transition with a charge-ordered phase. Both the found phases and the found phase transitions are accompanied by the extensive band-structure analysis that provided clarity and the understanding of the phase diagram. It is worth noting, that the quarter-filling for electrons ($n = 0.5$) and holes ($n = 1.5$) that is common for some organic conductors occurs in the M_{AAA} (FL), M^2_{ABB}, and M^2_{AAB} phases, which are not pinball-liquid phases within the MFA.

It is evident that the future investigation beyond the mean-field approximation can benefit from our analysis. Additionally, our research can easily be expanded to include next-nearest-neighbor interactions and finite temperatures. The more work is also required to include magnetic order and to consider the orderings that require larger supercells.

[1] F. Wu, T. Lovorn, E. Tutuc, and A. H. MacDonald, Hubbard model physics in transition metal dichalcogenide moiré bands, Phys. Rev. Lett. **121**, 026402 (2018).

[2] R. Bistritzer and A. H. MacDonald, Moiré bands in twisted double-layer graphene, PNAS **108**, 12233 (2011).

[3] F. Chen and D. N. Sheng, Singlet, triplet, and pair density wave superconductivity in the doped triangular-lattice moiré system, Phys. Rev. B **108**, L201110 (2023).

[4] K. Kim, A. DaSilva, S. Huang, B. Fallahazad, S. Larentis, T. Taniguchi, K. Watanabe, B. J. LeRoy, A. H. MacDonald, and E. Tutuc, Tunable moiré bands and strong correlations in small-twist-angle bilayer graphene, PNAS **114**, 3364 (2017).

[5] Y. Cao, V. Fatemi, V. Demir, S. Fang, S. L. Tomarken, J. Y. Luo, J. D. Sanchez-Yamagishi, K. Watanabe, T. Taniguchi, K. Kaxiras, R. C. Ashoori, and P. Jarillo-Herrero, Unconventional superconductivity in magic-angle graphene superlattices, Nature **556**, 80 (2018).

[6] Y. Cao, V. Fatemi, V. Demir, S. Fang, S. L. Tomarken, J. Y. Luo, J. D. Sanchez-Yamagishi, K. Watanabe, T. Taniguchi, K. Kaxiras, R. C. Ashoori, and P. Jarillo-Herrero, Correlated insulator behaviour at half-filling in magic-angle graphene superlattices, Nature **556**, 43 (2018).

[7] J. Yang, L. Liu, J. Mongkolkiattichai, and P. Schauss, Site-resolved imaging of ultracold fermions in a triangular-lattice quantum gas microscope, PRXQuantum **2**, 020344 (2021).

[8] J. Struck, C. Ölschläger, R. L. Targat, P. Soltan-Panahi, A. Eckardt, M. Lewenstein, P. Windpassinger, and K. Sengstock, Quantum simulation of frustrated classical magnetism in triangular optical lattices, Science **333**, 996 (2011).

[9] L. Mathey, S.-W. Tsai, and A. H. Castro Neto, Exotic superconducting phases of ultracold atom mixtures on triangular lattices, Phys. Rev. B **75**, 174516 (2007).

[10] D. Yamamoto, T. Fukuhara, and I. Danshita, Frustrated quantum magnetism with Bose gases in triangular opti-

cal lattices at negative absolute temperatures, Commun. Phys. **3**, 56 (2020).

[11] J. Mongkolkiattichai, L. Liu, D. Garwood, J. Yang, and P. Schauss, Quantum gas microscopy of fermionic triangular-lattice Mott insulators, Phys. Rev. A **108**, L061301 (2023).

[12] J. Wu, H. Tan, R. Cao, J. Yuan, and Y. Li, Orbital phases of p-band ultracold fermions in a frustrated triangular lattice, Phys. Rev. A **110**, 043319 (2024).

[13] S. Wessel, Simulations of atomic gases on frustrated optical lattices, Comput. Phys. Commun. **177**, 166 (2007).

[14] G.-B. Jo, J. Guzman, C. K. Thomas, P. Hosur, A. Vishwanath, and D. M. Stamper-Kurn, Ultracold atoms in a tunable optical kagome lattice, Phys. Rev. Lett. **108**, 045305 (2012).

[15] K. W. Kim and T. Pereg-Barnea, Interplay between superconductivity and magnetism in triangular lattices, Phys. Rev. B **108**, 195113 (2023).

[16] J. Venderley and E.-A. Kim, Density matrix renormalization group study of superconductivity in the triangular lattice Hubbard model, Phys. Rev. B **100**, 060506 (2019).

[17] K. S. Chen, Z. Y. Meng, U. Yu, S. Yang, M. Jarrell, and J. Moreno, Unconventional superconductivity on the triangular lattice Hubbard model, Phys. Rev. B **88**, 041103 (2013).

[18] H.-C. Jiang, Superconductivity in the doped quantum spin liquid on the triangular lattice, npj Quantum Materials **7**, 71 (2021).

[19] K. Horigane, K. Takeuchi, D. Hyakumura, R. Horie, T. Sato, T. Muranaka, K. Kawashima, H. Ishii, Y. Kubozono, S. Orimo, M. Isobe, and J. Akimitsu, Superconductivity in a new layered triangular-lattice system Li_2IrSi_2, New J. Phys. **21**, 093056 (2019).

[20] A. Yamada, d-wave superconductivity in the Hubbard model on the isotropic triangular lattice by the variational cluster approximation, J. Phys. Soc. Jpn. **94**, 044705 (2025).

[21] H. Watanabe and M. Ogata, Charge order and superconductivity in two-dimensional triangular lattice at $n = 2/3$, J. Phys. Soc. Jpn. **74**, 2901 (2005).

[22] J. Cheng, J. Bai, B. Ruan, P. Liu, Y. Huang, Q. Dong, Y. Huang, Y. Sun, C. Li, L. Zhang, Q. Liu, W. Zhu, Z. Ren, and G. Chen, Superconductivity in a layered cobalt oxychalcogenide Na_2CoSe_2O with a triangular lattice, J. Am. Chem. Soc. **146**, 5908 (2024).

[23] I. Morera, M. Kanász-Nagy, T. Smolenski, L. Ciorciaro, A. m. c. Imamoğlu, and E. Demler, High-temperature kinetic magnetism in triangular lattices, Phys. Rev. Research **5**, L022048 (2023).

[24] L. Ciorciaro, T. Smoleński, I. Morera, N. Kiper, S. Hiestand, M. Kroner, Y. Zhang, K. Watanabe, T. Taniguchi, E. Demler, and A. İmamoğlu, High-temperature kinetic magnetism in triangular lattices, Nature **623**, 509 (2023).

[25] J. Khatua, M. Pregelj, A. Elghandour, Z. Jagličic, R. Klingeler, A. Zorko, and P. Khuntia, Magnetic properties of the triangular-lattice antiferromagnets $ba_3RB_9O_{18}$ ($r = Yb, Er$), Phys. Rev. B **106**, 104408 (2022).

[26] G. Sala, M. B. Stone, S.-H. Do, K. M. Taddei, Q. Zhang, G. B. Halász, M. D. Lumsden, A. F. May, and A. D. Christianson, Structure and magnetism of the triangular lattice material $YbBO_3$, J. Phys.: Condens. Matter **35**, 395804 (2023).

[27] T. Ferreira, J. Xing, L. D. Sanjeewa, and A. S. Sefat, Frustrated magnetism in triangular lattice $TlYbS_2$ crystals grown via molten flux, Front. Chem. **8**, 127 (2020).

[28] M. O. Ogunbunmi and A. M. Strydom, Physical and magnetic properties of frustrated triangular-lattice antiferromagnets R_3Cu (R = Ce, Pr), J. Alloys Compd. **895**, 162545 (2022).

[29] J. Xing, L. D. Sanjeewa, J. Kim, G. R. Stewart, M.-H. Du, F. A. Reboredo, R. Custelcean, and A. S. Sefat, Crystal synthesis and frustrated magnetism in triangular lattice $CsRESe_2$ (RE = La–Lu): Quantum spin liquid candidates $CsCeSe_2$ and $CsYbSe_2$, ACS Materials Lett. **2**, 71 (2020).

[30] T. Isono, Y. Machida, and W. Fujita, Low-temperature magnetism in a triangular-lattice antiferromagnet, $Cu_3(OH)_4(HCO_2)_2$, studied by calorimetry, J. Phys. Soc. Jpn. **89**, 073707 (2020).

[31] T. Yoshioka, A. Koga, and N. Kawakami, Quantum phase transitions in the Hubbard model on a triangular lattice, Phys. Rev. Lett. **103**, 036401 (2009).

[32] T. Shirakawa, T. Tohyama, J. Kokalj, S. Sota, and S. Yunoki, Ground-state phase diagram of the triangular lattice Hubbard model by the density-matrix renormalization group method, Phys. Rev. B **96**, 205130 (2017).

[33] Y.-F. Jiang and H.-C. Jiang, Topological superconductivity in the doped chiral spin liquid on the triangular lattice, Phys. Rev. Lett. **125**, 157002 (2020).

[34] A. Szasz, J. Motruk, M. P. Zaletel, and J. E. Moore, Chiral spin liquid phase of the triangular lattice Hubbard model: A density matrix renormalization group study, Phys. Rev. X **10**, 021042 (2020).

[35] Y. Noda and M. Imada, Quantum phase transitions to charge-ordered and wigner-crystal states under the interplay of lattice commensurability and long-range coulomb interactions, Phys. Rev. Lett. **89**, 176803 (2002).

[36] K. Hiraki and K. Kanoda, Wigner crystal type of charge ordering in an organic conductor with a quarter-filled band: $(DI − DCNQI)_2Ag$, Phys. Rev. Lett. **80**, 4737 (1998).

[37] Y. Tan, P. K. H. Tsang, V. Dobrosavljević, and L. Rademaker, Doping a Wigner-Mott insulator: Exotic charge orders in transition metal dichalcogenide moiré heterobilayers, Phys. Rev. Research **5**, 043190 (2023).

[38] M. Matty and E.-A. Kim, Melting of generalized wigner crystals in transition metal dichalcogenide heterobilayer Moiré systems, Nat. Commun. **13**, 7098 (2022).

[39] Y. Kuramoto, Wigner crystal, electron chain, and charge density wave in strong magnetic fields, J. Phys. Soc. Jpn. **44**, 1572 (1978).

[40] M. Zarenia, D. Neilson, and F. M. Peeters, Inhomogeneous phases in coupled electron-hole bilayer graphene sheets: Charge density waves and coupled Wigner crystals, Sci. Rep. **7**, 11510 (2017).

[41] S. Pankov and V. Dobrosavljević, Self-doping instability of the wigner-mott insulator, Phys. Rev. B **77**, 085104 (2008).

[42] A. Amaricci, A. Camjayi, K. Haule, G. Kotliar, D. Tanasković, and V. Dobrosavljević, Extended hubbard model: Charge ordering and wigner-mott transition, Phys. Rev. B **82**, 155102 (2010).

[43] T. Mikolajick, S. Slesazeck, H. Mulaosmanovic, M. H. Park, S. Fichtner, P. D. Lomenzo, M. Hoffmann, and U. Schroeder, Next generation ferroelectric materials for semiconductor process integration and their applications, J. Appl. Phys. **129**, 100901 (2021).

[44] C. Hotta and N. Furukawa, Strong coupling theory of

the spinless charges on triangular lattices: Possible formation of a gapless charge-ordered liquid, Phys. Rev. B **74**, 193107 (2006).

[45] C. Hotta and N. Furukawa, Filling dependence of a new type of charge ordered liquid on a triangular lattice system, J. Phys.: Condens. Matter **19**, 145242 (2007).

[46] J. Merino, A. Ralko, and S. Fratini, Emergent heavy fermion behavior at the Wigner-Mott transition, Phys. Rev. Lett. **111**, 126403 (2013).

[47] A. Ralko, J. Merino, and S. Fratini, Pinball liquid phase from hund's coupling in frustrated transition-metal oxides, Phys. Rev. B **91**, 165139 (2015).

[48] F. Trousselet, A. Ralko, and A. M. Oleś, Valence bond crystal and possible orbital pinball liquid in a t_{2g} orbital model, Phys. Rev. B **86**, 014432 (2012).

[49] M. Miyazaki, C. Hotta, S. Miyahara, K. Matsuda, and N. Furukawa, Variational monte carlo study of a spinless fermion t–v model on a triangular lattice: Formation of a pinball liquid, Journal of the Physical Society of Japan **78**, 014707 (2009).

[50] M. Rakic, A. F. Ho, and D. K. K. Lee, Elastic properties and thermodynamic anomalies of supersolids, Phys. Rev. Res. **6**, 043040 (2024).

[51] R. Micnas, J. Ranninger, and S. Robaszkiewicz, Superconductivity in narrow-band systems with local nonretarded attractive interactions, Rev. Mod. Phys. **62**, 113 (1990).

[52] K. Rościszewski and A. M. Oleś, Charge order in the extended hubbard model, J. Phys.: Condens. Matter **15**, 8363 (2003).

[53] J. E. Hirsch, Charge-density-wave to spin-density-wave transition in the extended hubbard model, Phys. Rev. Lett. **53**, 2327 (1984).

[54] H. Q. Lin and J. E. Hirsch, Condensation transition in the one-dimensional extended hubbard model, Phys. Rev. B **33**, 8155 (1986).

[55] R. T. Clay, A. W. Sandvik, and D. K. Campbell, Possible exotic phases in the one-dimensional extended hubbard model, Phys. Rev. B **59**, 4665 (1999).

[56] K. Penc and F. Mila, Phase diagram of the one-dimensional extended hubbard model with attractive and/or repulsive interactions at quarter filling, Phys. Rev. B **49**, 9670 (1994).

[57] M. Calandra, J. Merino, and R. H. McKenzie, Metal-insulator transition and charge ordering in the extended hubbard model at one-quarter filling, Phys. Rev. B **66**, 195102 (2002).

[58] B. Davoudi and A.-M. S. Tremblay, Nearest-neighbor repulsion and competing charge and spin order in the extended hubbard model, Phys. Rev. B **74**, 035113 (2006).

[59] G. Litak and K. I. Wysokiński, Evolution of the charge density wave order on the two-dimensional hexagonal lattice, J. Magn. Magn. Mater. **440**, 104 (2017).

[60] M. Kaneko and M. Ogata, Mean-field study of charge order with long periodicity in θ-(BEDT-TTF) $_2$X, J. Phys. Soc. Jpn. **75**, 014710 (2006).

[61] S. F. Ung, J. Lee, and D. R. Reichman, Competing generalized Wigner crystal states in moiré heterostructures, Phys. Rev. B **108**, 245113 (2023).

[62] H. Pan, F. Wu, and S. Das Sarma, Quantum phase diagram of a Moiré-hubbard model, Phys. Rev. B **102**, 201104 (2020).

[63] A. Georges, G. Kotliar, W. Krauth, and M. J. Rozenberg, Dynamical mean-field theory of strongly correlated

fermion systems and the limit of infinite dimensions, Rev. Mod. Phys. **68**, 13 (1996).

[64] R. Pietig, R. Bulla, and S. Blawid, Reentrant charge order transition in the extended hubbard model, Phys. Rev. Lett. **82**, 4046 (1999).

[65] N.-H. Tong, S.-Q. Shen, and R. Bulla, Charge ordering and phase separation in the infinite dimensional extended hubbard model, Phys. Rev. B **70**, 085118 (2004).

[66] K. Kapcia and S. Robaszkiewicz, The effects of the next-nearest-neighbour density–density interaction in the atomic limit of the extended Hubbard model, J. Phys.: Condens. Matter **23**, 105601 (2011).

[67] K. Kapcia and S. Robaszkiewicz, On the phase diagram of the extended Hubbard model with intersite density–density interactions in the atomic limit, Physica A **461**, 487 (2016).

[68] K. Kapcia, S. Robaszkiewicz, M. Capone, and A. Amaricci, Doping-driven metal-insulator transitions and charge orderings in the extended Hubbard model, Phys. Rev. B **95**, 125112 (2017).

[69] K. J. Kapcia, Charge-order on the triangular lattice: A mean-field study for the lattice $s = 1/2$ fermionic gas, Nanomaterials **11**, 1181 (2021).

[70] K. J. Kapcia, Charge-order on the triangular lattice: Effects of next-nearest-neighbor attraction in finite temperatures, . Magn. Magn. Mater. **541**, 168441 (2022).

[71] T. Hanisch, G. S. Uhrig, and E. Müller-Hartmann, Lattice dependence of saturated ferromagnetism in the Hubbard model, Phys. Rev. B **56**, 13960 (1997).

[72] E. Kogan and G. Gumbs, Green's functions and DOS for some 2D lattices, Graphene **10**, 1 (2021).

[73] A. Cichy, K. J. Kapcia, and A. Ptok, Connection between the semiconductor-superconductor transition and the spin-polarized superconducting phase in the honeycomb lattice, Phys. Rev. B **105**, 214510 (2022).

[74] K. Momma and F. Izumi, VESTA3 for three-dimensional visualization of crystal, volumetric and morphology data, J. Appl. Crystallogr. **44**, 1272 (2011).

[75] See Supplemental Material at [URL will be inserted by publisher] with the results for band structure and evolution of various observables as a function of the model parameters.

Supplemental Material

Particle-Hole Asymmetry and Pinball Liquid in a Triangular-Lattice Extended Hubbard Model within Mean-Field Approximation

Aleksey Alekseev,[1] Agnieszka Cichy,[1,2] Konrad Jerzy Kapcia,[1]

[1]*Institute of Spintronics and Quantum Information, Faculty of Physics and Astronomy,*
Adam Mickiewicz University in Poznań, Uniwersytetu Poznańskiego 2, PL-61614 Poznań, Poland
[2]*Institut für Physik, Johannes Gutenberg-Universität Mainz, Staudingerweg 9, D-55099 Mainz, Germany*
(Dated: April 30, 2025)

In this Supplemental Material we present additional results which clarify the findings included in the main text and extend the discussion, in particular, concerning:

(i) the dependencies of various observables near phase transitions to supplement the discussion of the phase diagram (see Sec. S1 including the figures and multimedia description)

(ii) the full list of all transitions found in the system in the used approach (Sec. S2).

S1. THE DEPENDENCIES OF ORDER PARAMETERS AND GRAND-POTENTIAL CONTRIBUTIONS

Figures S1, S2, and S3 show the order parameters and the contributions in the grand potential as a function of V, $\bar{\mu}$, and U, respectively. The metastability of the phases (hysteresis) is also shown with dotted lines. In some cases the spectral weight at the Fermi level ($A(i\eta)$) is shown on two different scales due to its proximity to a spectral-weight singularity in the M^1_{ABB} and M_{ABC} phases. In particular, the figures contain the results for the following model parameters:

- Fig. S1 shows V-dependencies for $U = 2.00D$ and various values of $\bar{\mu}$: (a) $\bar{\mu} = -3.00D$, (b) $\bar{\mu} = 3.00D$, (c) $\bar{\mu} = -1.25D$, (d) $\bar{\mu} = -0.30D$, and (e) $\bar{\mu} = 1.00D$;

- Fig. S2 shows $\bar{\mu}$-dependencies for (a) $U = 0.00D$ and $zV = 3.50D$, (b) $U = 0.00D$ and $zV = 4.00D$, and (c) $U = 2.00D$ and $zV = 7.00D$;

- Fig. S3 shows U-dependencies for (a) $\bar{\mu} = -3.00D$ and $zV = 4.00D$, (b) $\bar{\mu} = 3.00D$ and $zV = 4.00D$, (c) $\bar{\mu} = -0.30D$ and $zV = 5.50D$, and (d) $\bar{\mu} = 0.00D$ and $zV = 9.00D$.

In addition, we present nine multimedia movies that show the evolution of the band structure and density of states:

1. `M1_U2.00_V3.50_AAB.mp4`
   — evolution between $\bar{\mu} = 1.50D$ and $\bar{\mu} = 2.60D$ for $U = 2.00D$ and $zV = 3.50D$ (transitions M^1_{AAB}-I_{AAB} and I_{AAB}-M^2_{AAB})

2. `M2_U2.00_mu2.00_AAB.mp4`
   — evolution between $zV = 3.50D$ and $zV = 9.00D$ for $U = 2.00D$ and $\bar{\mu} = 2.00D$

3. `M3_U2.00_V3.50_ABB.mp4`
   — evolution between $\bar{\mu} = -2.38D$ and $\bar{\mu} = -1.20D$ for $U = 2.00D$ and $zV = 3.50D$ (transitions M^2_{ABB}-I_{ABB} and I_{ABB}-M^1_{ABB})

4. `M4_U2.00_mu-1.80_ABB.mp4`
   — evolution between $zV = 3.50D$ and $zV = 9.00D$ for $U = 2.00D$ and $\bar{\mu} = -1.80D$

5. `M5_U2.00_mu-0.85_ABB_SymBreak.mp4`
   — evolution between $zV = 2.95D$ and $zV = 3.45D$ for $U = 2.00D$ and $\bar{\mu} = -0.85D$ (transition M_{AAA}-M^1_{ABB})

6. `M6_U2.00_mu-0.80_AAB_SymBreak.mp4`
   — evolution between $zV = 2.95D$ and $zV = 3.45D$ for $U = 2.00D$ and $\bar{\mu} = -0.80D$ (transition M_{AAA}-M^1_{AAB})

7. `M7_U2.00_mu-1.80_ABB_SymBreak.mp4`
   — evolution between $zV = 2.95D$ and $zV = 3.45D$ for $U = 2.00D$ and $\bar{\mu} = -1.80D$ (transitions M_{AAA}-M^2_{ABB} and M^2_{ABB}-I_{ABB})

8. `M8_U0.00_mu3.10_AAB_SymBreak.mp4`
   — evolution between $zV = 2.35D$ and $zV = 2.85D$ for $U = 0.00D$ and $\bar{\mu} = 3.10D$ (transition I_{222}-M^2_{AAB})

9. `M9_U2.00_V4.40_ABB-ABC-AAB.mp4`
   — evolution between $\bar{\mu} = -0.70D$ and $\bar{\mu} = -0.10D$ for $U = 2.00D$ and $zV = 4.40D$ (transitions M^1_{ABB}-M_{ABC} and M_{ABC}-M^1_{AAB})

S2. TRANSITIONS FOUND IN THE SYSTEM

The list of 24 phase transitions:

1. ABB-metal-insulator transitions (blue region):

   1.1 M^1_{ABB} to I_{ABB} (continuous);
   1.2 M^2_{ABB} to I_{ABB} (continuous);

2. AAB-metal-insulator transitions (yellow region):

   2.1 M^1_{AAB} to I_{AAB} (continuous);
   2.2 M^2_{AAB} to I_{AAB} (continuous);
   2.3 M^2_{AAB} to I_{AAB} (discontinuous), for large $\bar{\mu}$ but small U;

3. FL to ABB transitions (red to blue):

   3.1 M_{AAA} to M^1_{ABB} (discontinuous);
   3.2 M_{AAA} to M^1_{ABB} (continuous), a small region in the very proximity of M^1_{ABB}-M^1_{AAB} transition;
   3.3 M_{AAA} to M^2_{ABB} (discontinuous), not for small U;
   3.4 M_{AAA} to M^2_{ABB} (continuous), a small region, not for small U;
   3.5 M_{AAA} to I_{ABB} (discontinuous);

4. FL to AAB transitions (red to yellow):

   4.1 M_{AAA} to M^1_{AAB} (discontinuous);
   4.2 M_{AAA} to M^1_{AAB} (continuous), a small region in the very proximity of M^1_{ABB}-M^1_{AAB} transition;
   4.3 M_{AAA} to M^2_{AAB} (discontinuous);
   4.4 M_{AAA} to I_{AAB} (discontinuous);

5. M^1_{ABB}-M^1_{AAB} transition (blue to yellow) (discontinuous);

6. ABC region (blue-white-yellow):

   6.1 M_{ABC} to M^1_{ABB} (continuous);
   6.2 M_{ABC} to M^1_{AAB} (continuous);
   6.3 inside the M_{ABC} the discontinuous transition from ABB-like M_{ABC} phase to AAB-like M_{ABC} phase. As shown on phase diagram, there is a region where this transition disappears (the line is terminated)
   6.4 directly from AAB-like M_{ABC} phase to M^1_{ABB} phase (discontinuous);

7. The M^1_{AAB} phase is not a PL as it gets closer to M^1_{ABB}-M_{AAA}-M^1_{AAB} triple point. The approximate border between M^1_{AAB}-PL and M^1_{AAB}-non-PL is the dotted line;

8. In the limit of large V, the M^1_{ABB} phase becomes a PL because the hybridization between triangular and honeycomb lattices disappears, but the border of this phase is hard to define;

9. Additionally, there is one transition from FL to the fully unoccupied phase, and two transitions to the fully occupied phase: from FL and directly from M^2_{AAB} phase.
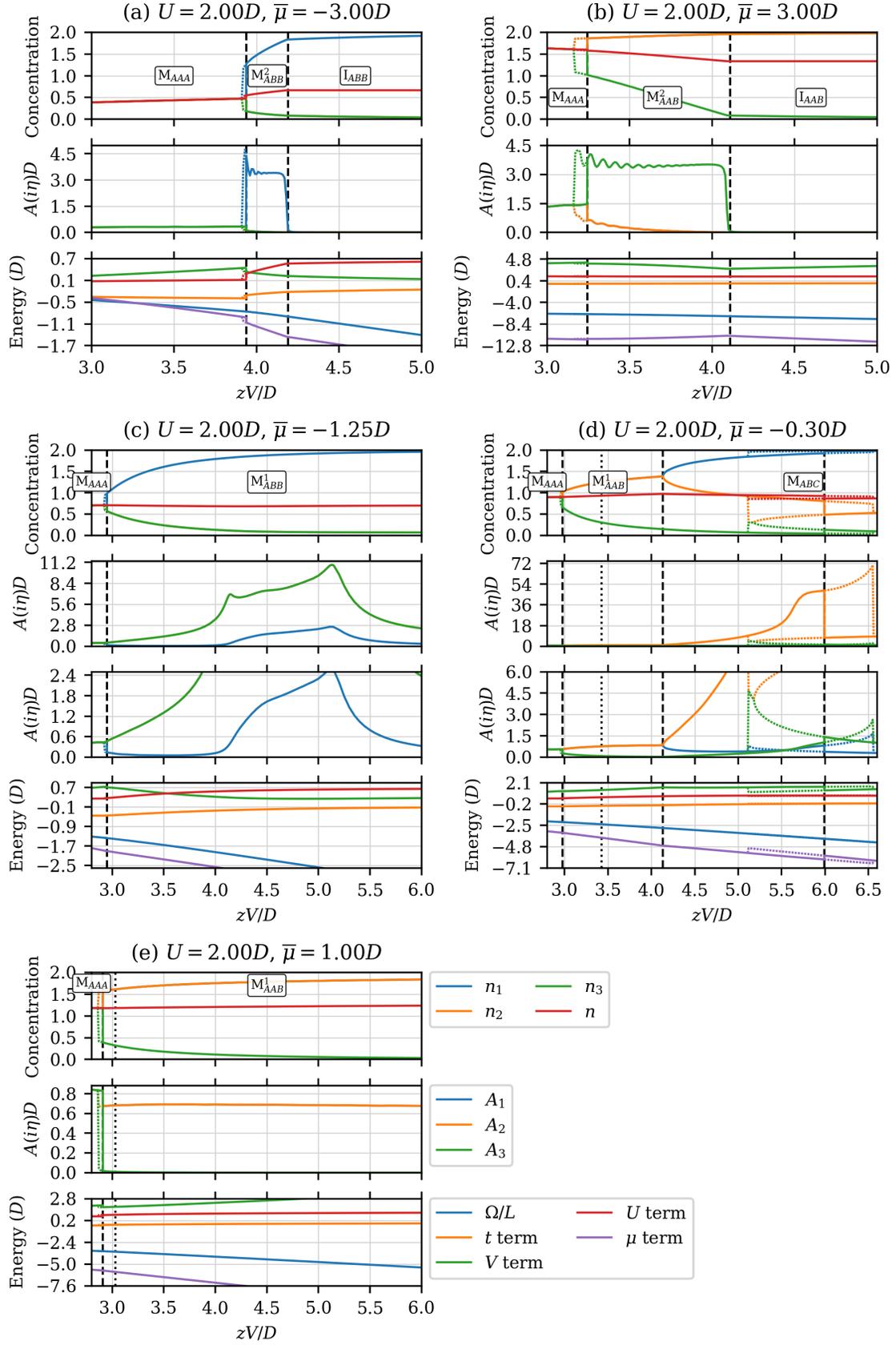
FIG. S1. The order parameters and the grand-potential contributions as a function of V for $U = 2.00D$ and representative values of $\bar{\mu}$ (as labeled). The black dashed vertical lines show the location of phase transitions, the black dotted vertical line corresponds to the dotted line in Fig. 2 in the main text, where the M^1_{AAB} phase is not a PL anymore.
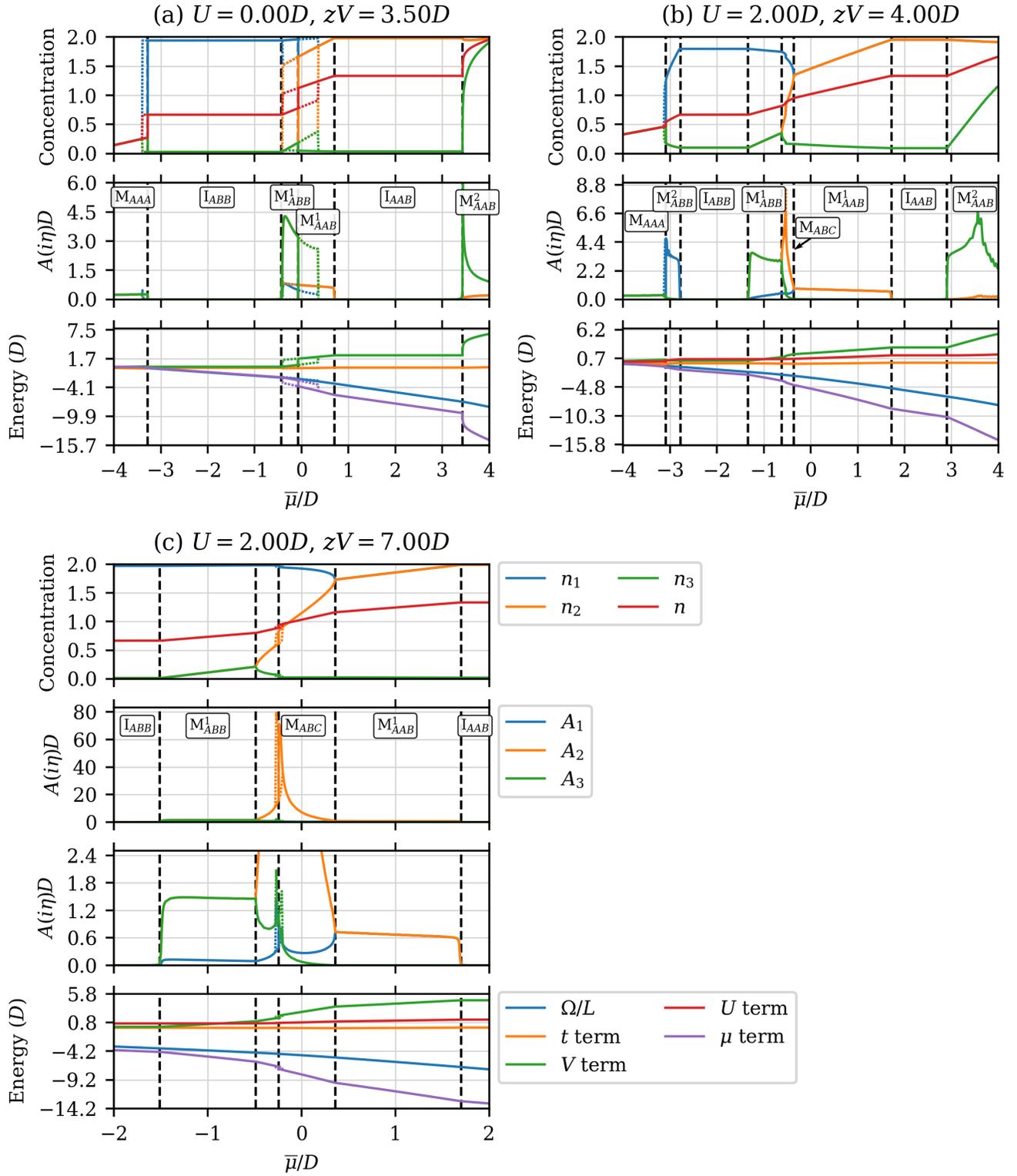
FIG. S2. The order parameters and the grand-potential contributions as a function of $\bar{\mu}$ for representative values of U and V (as labeled). The black dashed vertical lines show the location of phase transitions.
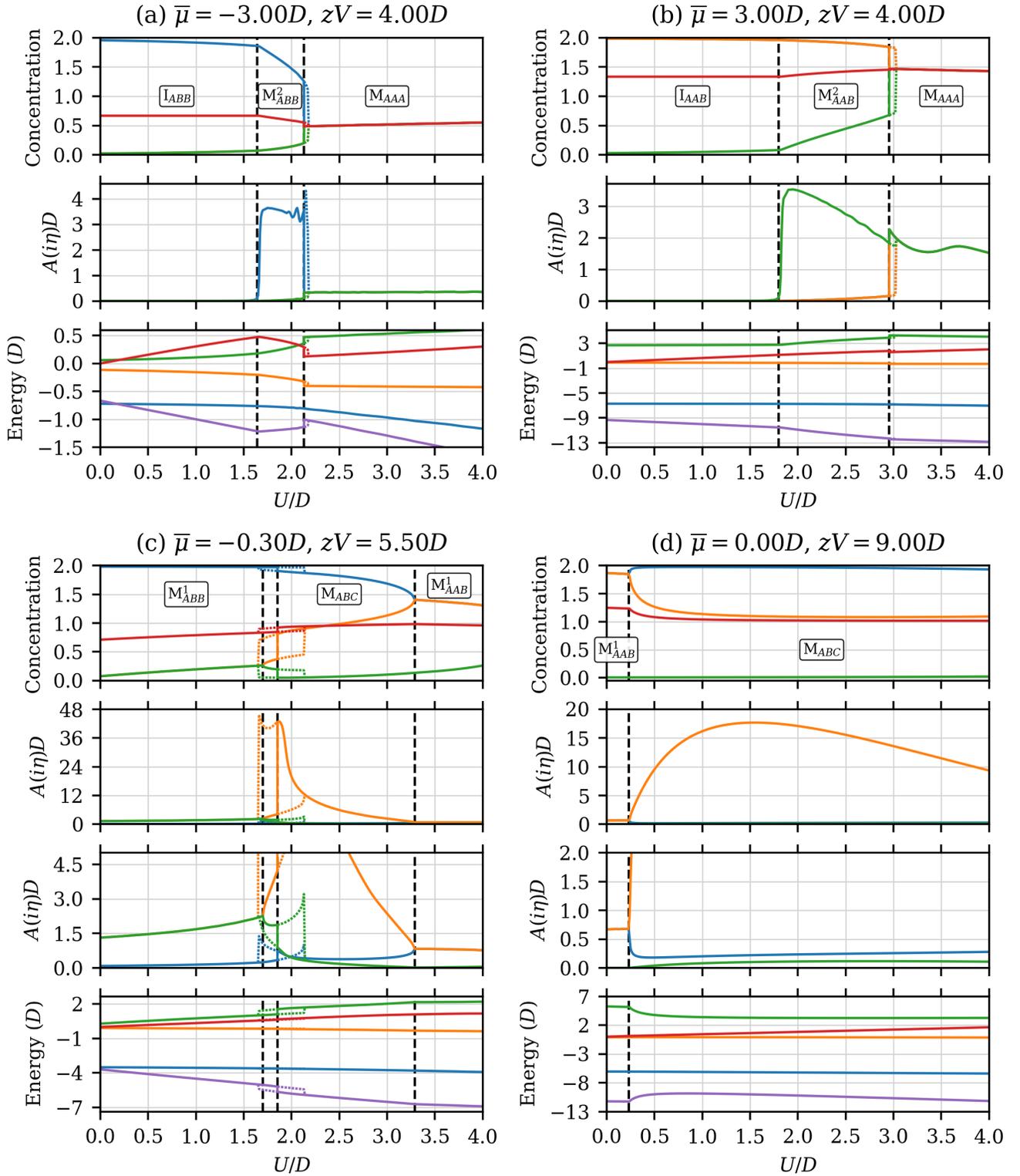
FIG. S3. The order parameters and the grand-potential contributions as a function of U for representative values of $\bar{\mu}$ and V (as labeled). The black dashed vertical lines show the location of phase transitions. The legend is the same as in Figs. S1 and S2.